ARGONNE NATIONAL LABORATORY
9700 South Cass Avenue, Argonne Illinois 60439

ANL-ET/02-26

HYDRODYNAMIC PHENOMENA OF GAS-FILLED CHAMBER DUE TO TARGET IMPLOSION IN FUSION REACTORS

By
V. Sizyuk and A. Hassanein
Energy Technology Division

July 2002

Argonne National Laboratory, a U.S. Department of Energy Office of Science laboratory, is operated by The University of Chicago under contract W-31-109-Eng-38.

Available electronically at http://www.doe.gov/bridge

Available for a processing fee to U.S. Department of Energy and its contractors, in paper, from:

U.S. Department of Energy
Office of Scientific and Technical Information
P.O. Box 62
Oak Ridge, TN 37831-0062
phone: (865) 576-8401
fax: (865) 576-5728
email: reports@adonis.osti.gov

CONTENTS

FIGURES

Hydrodynamic Phenomena of Gas-Filled Chamber Due to Target Implosion in Fusion Reactors

by

V. Sizyuk and A. Hassanein

Abstract

Use of an intermediate gas in the reaction chamber of an inertial fusion power reactor is under consideration to decrease the thermal shock to the walls resulting from target implosions. A model was developed and implemented in HEIGHTS package to simulate hydrodynamic and radiation shock waves in the chamber and used to determine the effect of xenon gas at various densities ranging from mtorr up to tens of torr. Numerical calculations for the dense-gas case indicated that two pressure peaks result from the shock wave interacting with the chamber wall, and radiation energy accumulates directly in front of the hydrodynamic shock wave. The shock wave should reach a maximum pressure peak when the chamber gas has a density between the two extremes analyzed. In general, calculated results with our model compared favorably with previously published data.

1. Introduction

The chamber walls in inertial fusion energy (IFE) reactors are exposed to harsh conditions following each target implosion. Key issues of the cyclic IFE operation include: intense photon and ion deposition, wall thermal and hydrodynamic evolution, wall erosion and fatigue lifetime, and chamber clearing and evacuation to ensure chamber conditions prior to target implosion. In the past, several methods for wall protection have been proposed, each having its own advantages and disadvantages. These include solid bare walls, gas-filled cavities, and liquid walls/jets. Detailed models are developed for reflected laser light, emitted photon, and target debris deposition and interaction with chamber components and implemented in the comprehensive HEIGHTS package. Hydrodynamic response of gas-filled cavities and photon radiation transport of the deposited energy is calculated in detail using new and advanced numerical techniques for accurate evaluation.

The overall objective of this proposed task is to create a fully integrated model within the frame of the HEIGHTS package to study chamber dynamic behavior after target implosion. This includes cavity gas hydrodynamics; the particle/radiation interaction; the effects of various heat

sources such as direct particle and debris deposition, gas conduction and convection, radiation transport; chamber wall response and lifetime; and the cavity clearing. The model focuses on the relatively long-time phenomena following the target blast up to the chamber clearing in preparation for the next target injection. This should include both micro and macroscopic particles (i.e., mechanisms of generation, dynamics, vaporization, and condensation and deposition due to various heat sources: direct laser/particle beam, debris and target conduction, convection, and radiation). These processes are detrimental and of significant importance to the entire success of inertial fusion power reactors.

Interpretation of the initial results from these calculations poses some challenges. For example, the numerical calculations require very small time steps for the artificial uniform deposition of energy in any central area of the chamber. Further, initial abrupt gradients of some parameters along with uniform gradients of others do not describe a real physical situation. Finally, the numerical scheme needs time in relaxing to the normal state. This process can be the source of additional instabilities in solving the hydrodynamic and radiation transport problems. In this report, energy deposition is initiated in the chamber by simulation of real target X-ray flux. The model below describes the generation and propagation of shock waves in the chamber-gas Xe for a closely-coupled heavy ion-beam (HIB) target explosion (115 MJ X-ray) and is used to determine its influence on the first-wall radiation flux.

2. Physical Description

As an example for modeling the X-ray output source as a result of target implosion, we used a closely-coupled HIB target with total deposited energy of 115 MJ in 10 nsec. The spectrum of this target is described using a "three-temperature" fit equation [6]:

$$E(T) = \frac{c_1 T^3}{\exp(T/T_1) - 1} + \frac{c_1 T^3}{\exp(T/T_2) - 1} + \frac{c_1 T^3}{\exp(T/T_3) - 1} \left[J/keV \right] \tag{1}$$

where T is photon energy in keV, and the coefficients for the HIB target output spectra are::

c1 =5.73·109 J/keV4, T1 =0.183 keV

c2 =5.84·107 J/keV4, T2 =0.65 keV (2)

c3 =38.9 J/keV4, T3 =12.0 keV

Figure 1 shows the calculated X-ray spectra using the above equation. This figure agrees well with that presented in Ref. [6]. The main goal of our simulation was ell by using real-time and spectrum parameters. The spectrum of radiation was divided into 1350 groups of photon energies. Total radiated energy was calculated for each group. We assumed uniform X-ray flux over time.

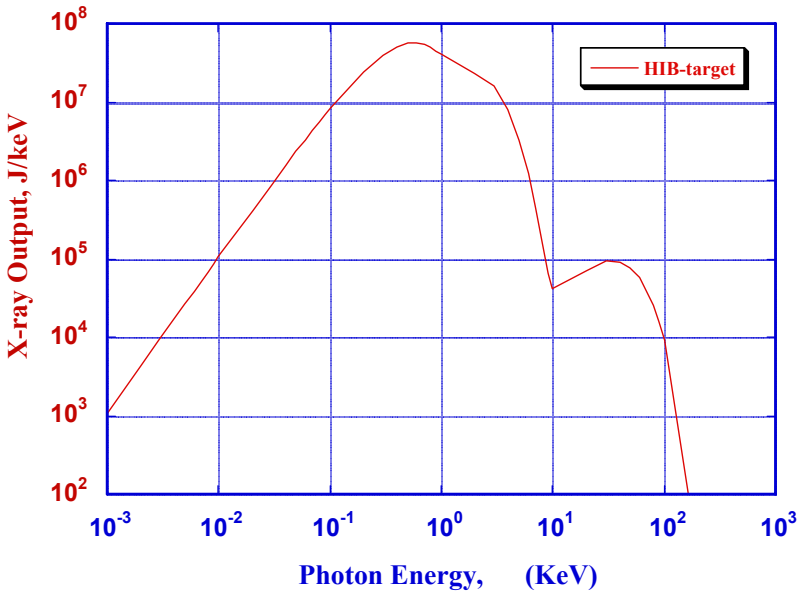

Fig. 1 Spectrum calculated by "three-temperature" fit equation for HIB target

In this way, it is possible to consider additional flux with calculated energy distribution in the central cell. According to the developed algorithm, generated fluxes were angle averaged and the energy deposition was determined in time steps. Note that in the described problem, the target radiation warms the whole chamber except for the first cells in the model, and energy deposition does not occur in the center of the ball formed by the shock wave. To correct this case, we have made hyperbolic extrapolations of the first-cell total energy at each time step. We used energy data from adjacent cells for this correction. Extrapolation of energy in the first cell is over by the end of target implosion (10 nsec). The initial distribution of deposited energy is

formed at this moment, and thus we have a good approximation for describing the X-ray source. Figure 2 shows a schematic illustration of the initial distribution of energy and pressure in the chamber gas after target implosion.

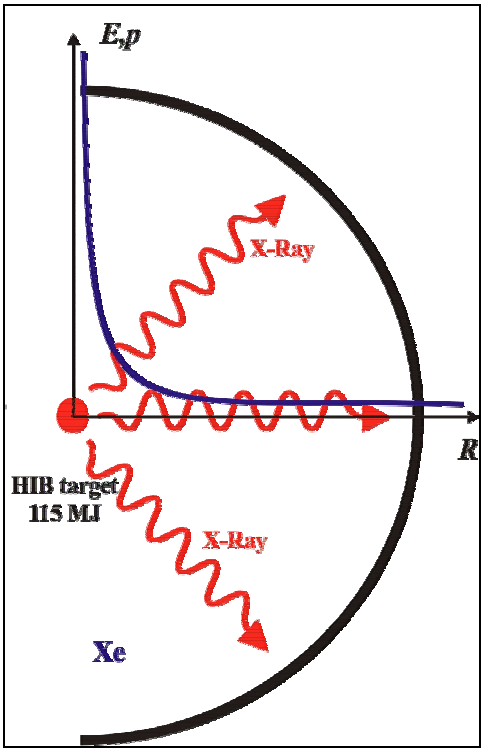

Fig. 2 Scheme of initial conditions for numerical calculations

The density and temperature of the working gas will determine the conditions of radiation propagation and the magnitude of the energy deposited in the gas and at the wall. For our calculations and to compare with previously published results, we studied three cases [7]: (1) 3.0-m chamber radius and 23 torr Xe gas pressure, (2) 4.5-m chamber radius and 0.96 torr Xe gas pressure and (3) 6.5-m chamber radius and 0.21 torr Xe gas pressure. Figures 3 and 4 plot radiation flux in the initial time moment divided by photon energy groups, for cases 1 and 3 respectively. The heavy X-ray absorption in case 1 for the high-density Xe, is desirable since it will reduce the direct energy deposited at the wall. These curves were calculated with the forward-reverse radiation transport method without taking into account detail lines distribution.

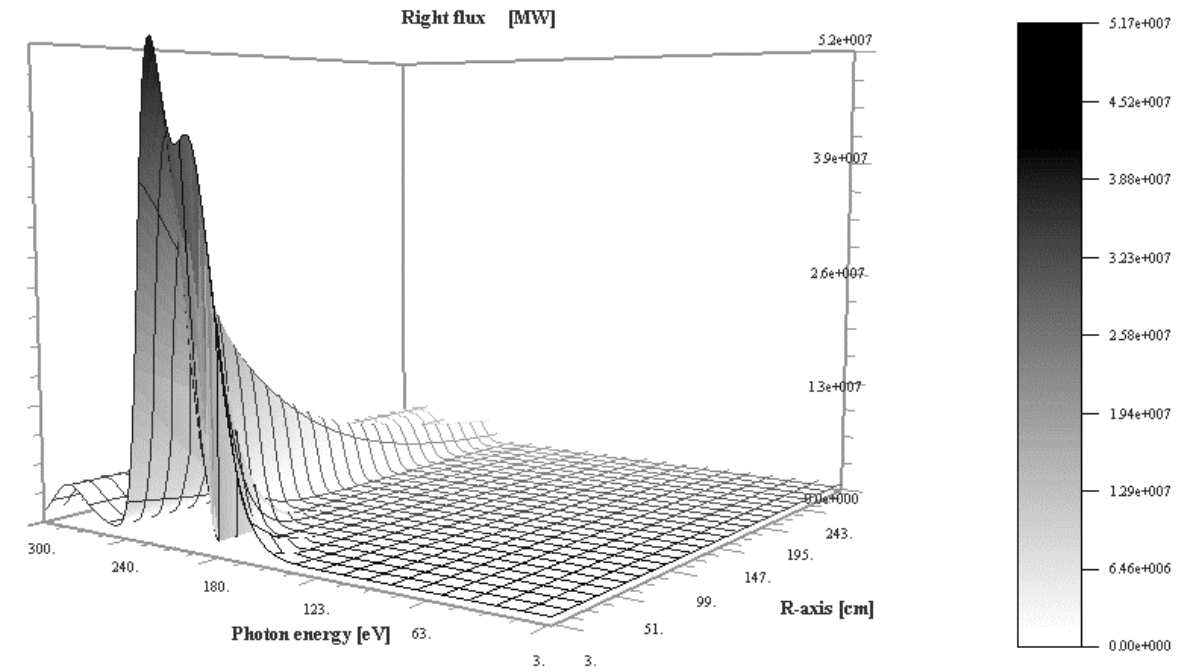

Fig. 3 Target behavior for the dense chamber gas (23 torr Xe).

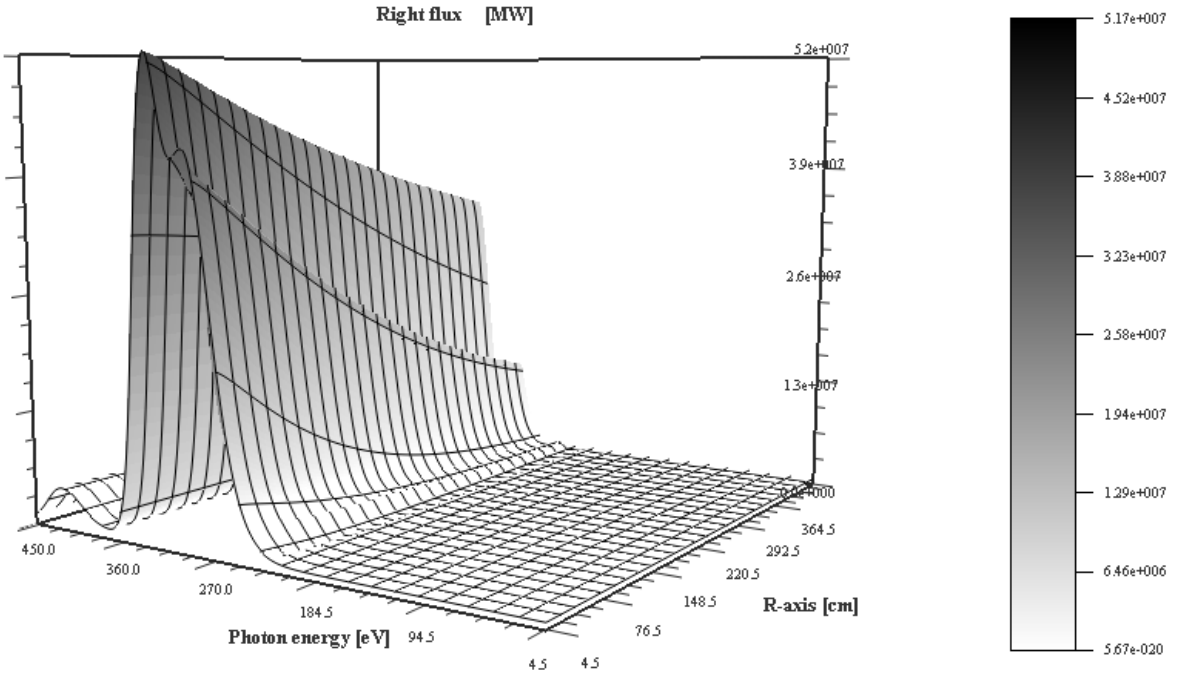

Fig. 4 - Target behavior for the rarefied chamber gas (0.21 torr Xe).

3. Calculation Methods

Hydrodynamic calculations were performed with the TFD-LF formulation. The TVD schemes ensure that the total variation in the calculating area ΔX does not increase with time [2]:

$$\sum_j \left|\Delta \hat{u}^{n+1}_{j+1/2}\right| \le \sum_j \left|\Delta \hat{u}^{n}_{j+1/2}\right| \quad (3)$$

The usual method of predictor-corrector algorithm is unstable and requires the addition of an energy dissipation mechanism at the front of the shock waves. This mechanism can be artificial diffusion, increased viscosity, etc. The coefficients for these mechanisms can be adjusted to obtain better results, but that problem-dependent approach is not in the spirit of modern shock-wave capturing schemes. The TVD method is a part of the essentially non-oscillatory (ENO) schemes. There is no generation of nonphysical oscillations along the shock waves in these schemes. Mechanisms of numerical dissipation with controlled automatic feedback allow transformation of shock-wave kinetic energy into heat energy. It is even possible to solve shock-wave problems within 2-4 cells only.

The gas-dynamics equations in spherical coordinates are

$$\begin{cases} \dfrac{\partial \rho}{\partial t} + \dfrac{1}{r^2}\dfrac{\partial}{\partial r}\left(r^2 \rho V_r\right) = 0 \\ \dfrac{\partial (\rho V_r)}{\partial t} + \dfrac{1}{r^2}\dfrac{\partial}{\partial r}\left(r^2 \rho V_r^2\right) + \dfrac{\partial p}{\partial r} = 0 \\ \dfrac{\partial e}{\partial t} + \dfrac{1}{r^2}\dfrac{\partial}{\partial r}\left(r^2 V_r (p+e)\right) = 0 \end{cases} \quad (4)$$

The same in matrix form is:

$$\frac{\partial U}{\partial t} + \frac{1}{r^2}\frac{\partial}{\partial r}\left[r^2 F(U)\right] + \frac{\partial P(U)}{\partial r} = 0 \quad (5)$$

In these equations,

$$U = \begin{bmatrix} \rho \\ \rho V_r \\ e \end{bmatrix}, \qquad F = \begin{bmatrix} \rho V_r \\ \rho V_r^2 \\ V_r(p+e) \end{bmatrix}, \qquad P = \begin{bmatrix} 0 \\ p \\ 0 \end{bmatrix} \tag{6}$$

where

ρ - density [g/cm3],

V_r - radial velocity [cm/sec],

p - pressure [dyne/cm2],

e - total energy [erg/cm3].

For a closed system (1), one can use the ideal gas equations

$$V_{ac} = \sqrt{\frac{\gamma p}{\rho}}, \quad p = (\gamma - 1)\left(e - \frac{\rho V_r^2}{2}\right), \quad T = \frac{M_{gas} p}{\rho R} \tag{7}$$

or the real thermodynamic properties of the gas taken from published tables. In our calculations we used the real properties of Xe gas calculated for the chamber condition with collisional-radiative equilibrium (CRE) model. Two TVD methods exist for numerical calculation of the system (2): monotonic-upwind-schemes-for-conservation-laws (MUSCL) and non-MUSCL. The non-MUSCL method is based on characteristic waves and uses the c^k eigenvalues and the r^k right and l^k left eigenvectors of the $\partial F / \partial U$ matrix. It requires considerable calculational time consumption, especially if the real thermodynamic properties of the gas are used. Furthermore, this method does not work well for calculating strong rarefaction waves. TVD-LF correction is one of the MUSCL schemes. TVD-LF does not use a Riemann solver and can be applied to any system of conservation laws without knowledge of the characteristic waves. Maximum propagation speed of information is used for the definition corrector function; in this case, $c_r^{\max} = |v_r| + \sqrt{\frac{\gamma p}{\rho}}$.

A full numerical algorithm with difference scheme for the 1D spherical case solved by TVD-LF is given in the appendix. It is necessary to explain the basis of the TVD method, slope limiters. Slope limiters are used in TVD-LF for calculation of ΔU differences for conservative variables and provide the mechanism of energy dissipation between model cells. The simplest slope limiter can be defined by a minmod function which can be written for any variables w1, w2,…,wn. as

$$\min \mathrm{mod}(w_1, w_2, ..., w_n) = \mathrm{sgn}(w_1)\max\left[0, \min\left(|w_1|, \mathrm{sgn}(w_1)w_2, ..., \mathrm{sgn}(w_1)w_n\right)\right].$$

A minmod function with two variables is also used in TVD-LF for calculating fluxes at the cell borders. The core of HEIGHTS-IFE hydrodynamic package was developed based on the methods briefly described by the above principles. It was written and tested for the 2-D cylinder geometry, and 1-D spherical geometry. Three-dimensional code for rectangular Cartesian geometry is under construction.

The 2-D package was tested using the standard problem of flow around a sphere. For this purpose, a technique was developed for separate compensation of the flow along coordinate axes. This technique is based on formulation of separate boundary conditions for each spatial direction during the course of field calculations. With such technique, the TVD-LF method allows one to use a rectangular grid for simulation of the flow around arbitrarily shaped regions. This feature avoids the implementation of a curvilinear coordinate system that has coordinate lines (surfaces) coincident with all boundaries. It is known that incorporation of unstructured grids into a code has a significant effect on calculation complexity and computational time.

To validate the package and to test implemented models, supervelocity flow around a sphere was computed and compared to published experimental data. Figure 5 shows the excellent agreement between experimental data [8] and the present computation of density distribution in the shock wave before a sphere. Good agreement has also been obtained between computation (Fig. 6) and the experimental data of Van Dyke [9] for the shock wave shape and stand off distance. Reasonable agreement was attained for the flow structure.

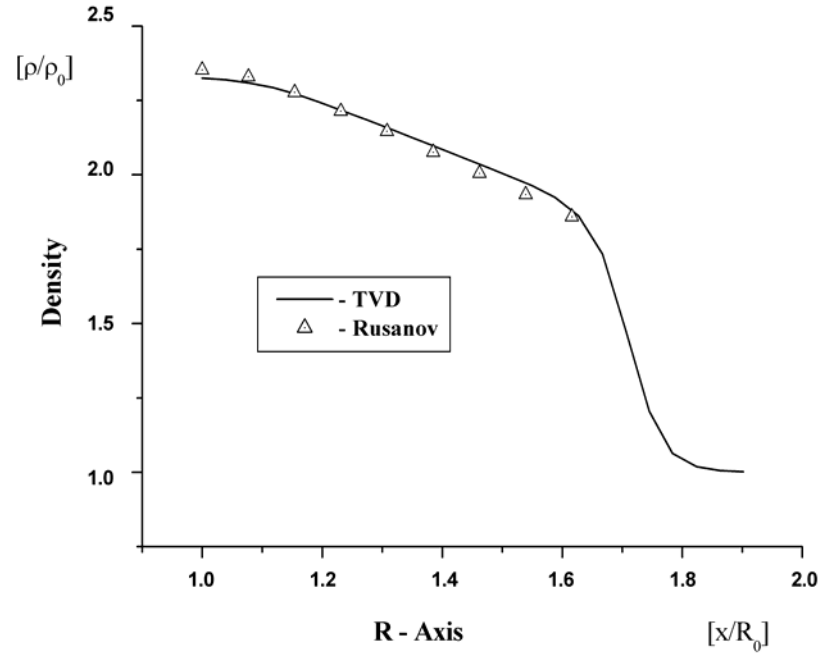

Figure 5 - Comparison of of TVD-LF curve with experimental data of Lubimov and Rusanov [8]. Shock wave is due to 1.5 M flow around a sphere.

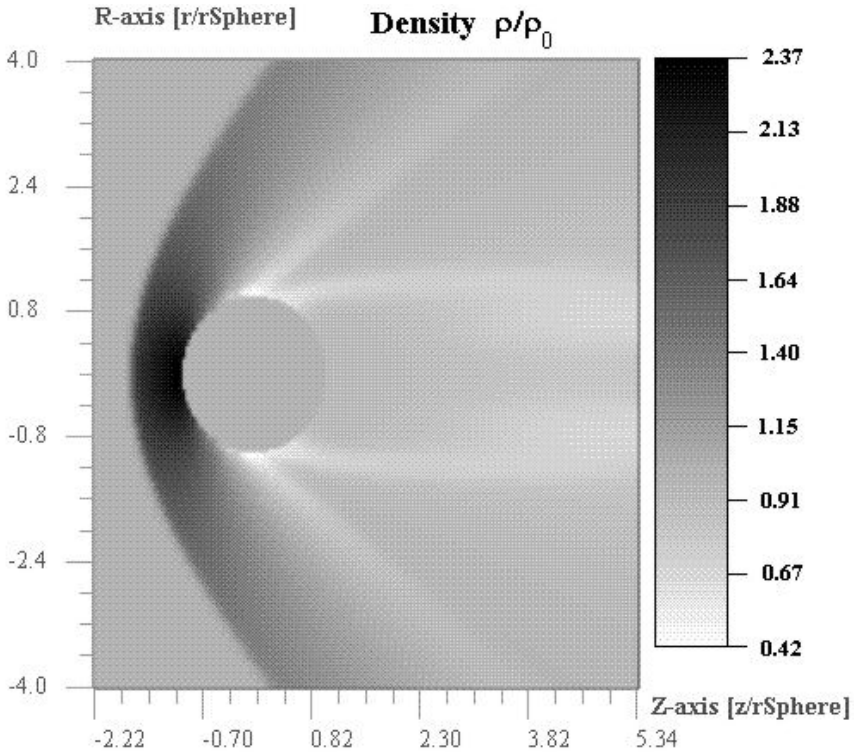

Fig. 6 Steady-state density field due to 1.53 M flow around a sphere calculated by TVD-LF.

4. Hydrodynamic Phenomena

Generation of the shock wave starts in the Xe chamber gas as a result of gradient energy deposition. An area of high pressure is formed at the chamber center. Gas particles appear near the center of the shock acceleration. Subsequent evolution of this acceleration strongly depends on the initial Xe density. For this reason, we considered two gas variants: a dense (case 1) and a rarefied gas (cases 2 and 3).

The initial energy deposition (and pressure) is higher in the denser gas. As a result the initial acceleration of the shock wave is also higher. The 5-μsec curves in Figs. 7-9 confirm this conclusion. The velocity distributions for 10, 30, and 50 μsec show higher deceleration of wave propagation in the denser gas. Since the acoustic velocity is less in the denser gas, supersonic flow in case 1 (Fig. 10) is much higher than in cases 2 and 3 (Figs. 11 and 12).

Photon radiation transport has an important effect on the hydrodynamics of a dense gas. The emitted photon radiation behind the shock wave is absorbed in front of the wave. Heating of the gas occurs at a distance of the quantum free path from the shock wave and subsides in consequence of radiation flux absorption. The shock wave propagates in the heated gas. In contrast to the rarefied gas cases, the temperature is higher before the wave and usually is lower after the wave. Front gas heating brings about a pressure increase and deceleration of the gas in the shock-wave coordinate system. The system is thus closed: radiation transport influences on the hydrodynamics and the hydrodynamics influences the radiation. The gas particles absorb additional energy in the front shock wave and lose it after the front.

This equilibrium is, however, disturbed when the heated area arrives at the wall. In cases 2 and 3, the above-described processes are feebly present. The 0.96 and 0.21 torr Xe gas is transparent enough for radiation, and energy deposition in the front wave is small.

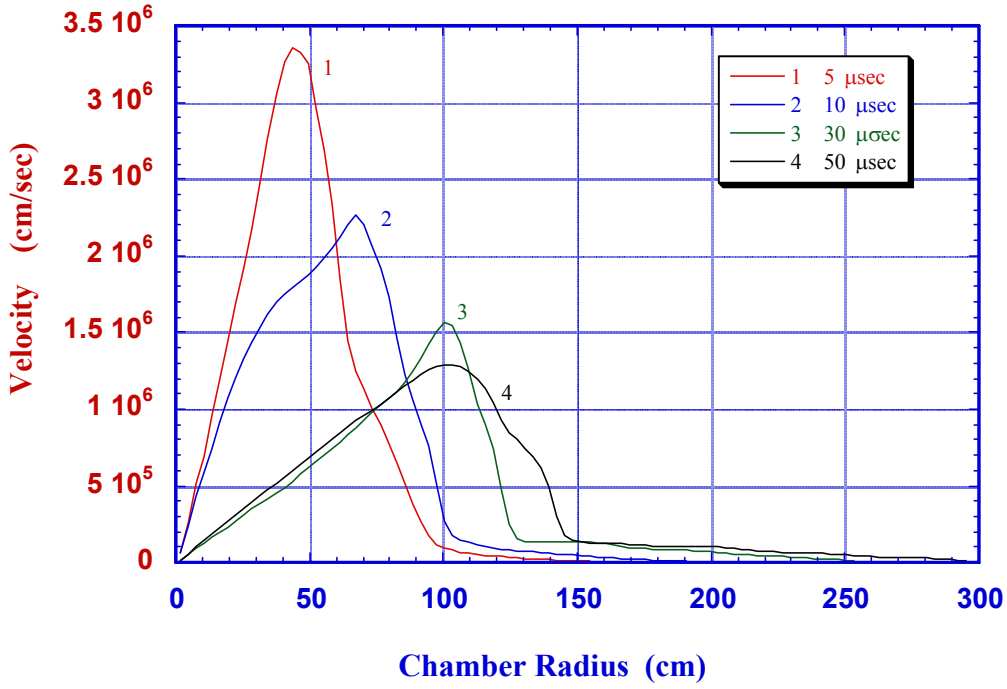

Fig. 7 Velocity evolution by generation of shock wave in the 3.0-m chamber for HIB target (115 MJ) with 23 torr Xed

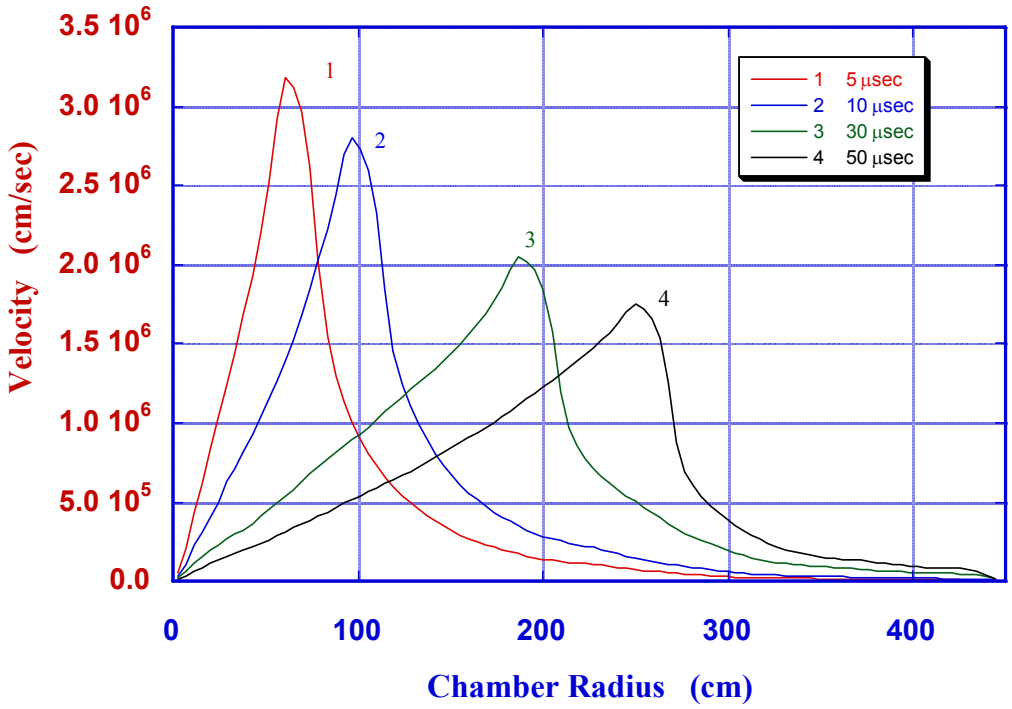

Fig. 8 Velocity evolution by generation of shock wave in the 4.5-m chamber for HIB target (115 MJ) with 0.96 torr Xe

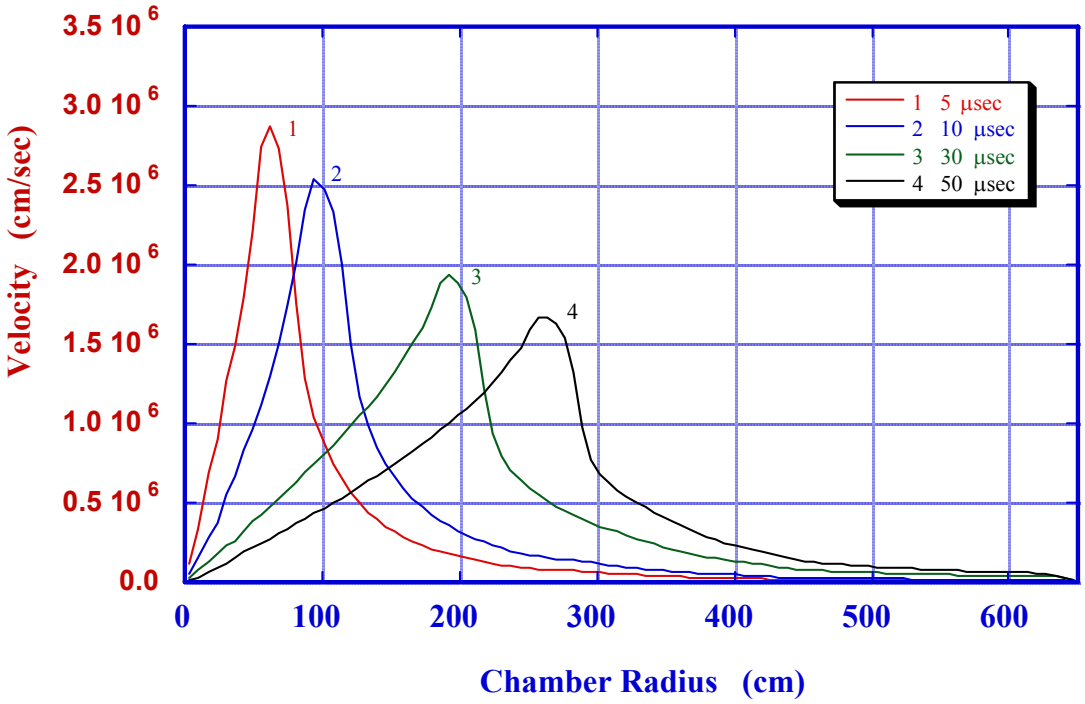

Fig 9 Velocity evolution by generation of shock wave in the 6.5-mchamber for HIB target (115 MJ) with 0.21 torr Xe.

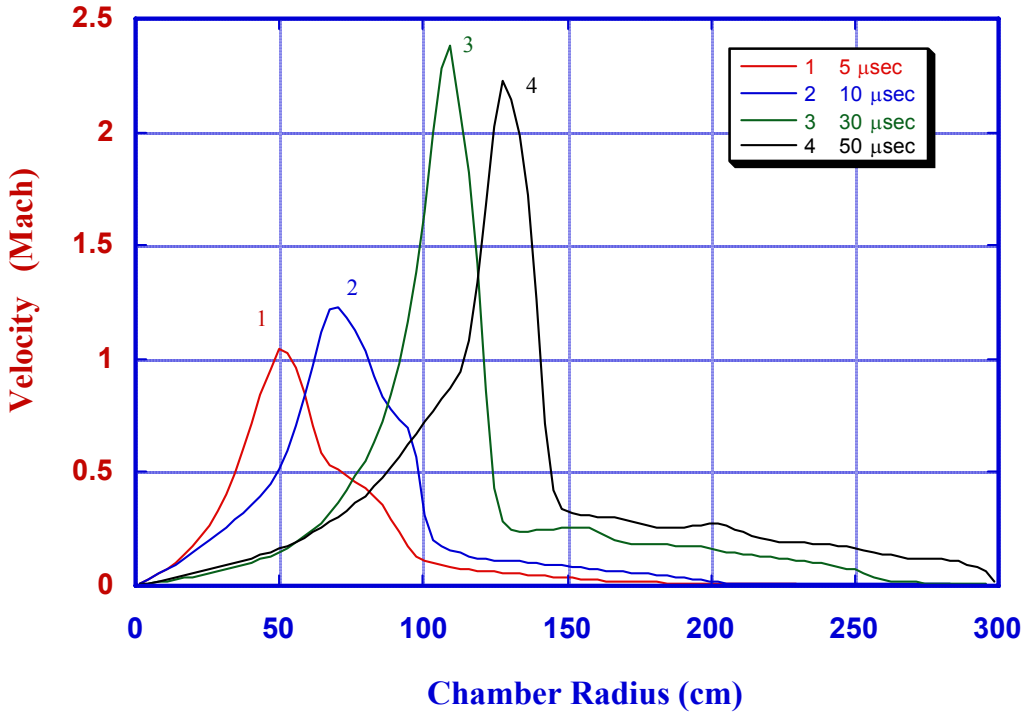

Fig. 10 Generation of supersonic wav in 3.0-m chamber for HIBtarget (115 MJ) with 23 torr Xe

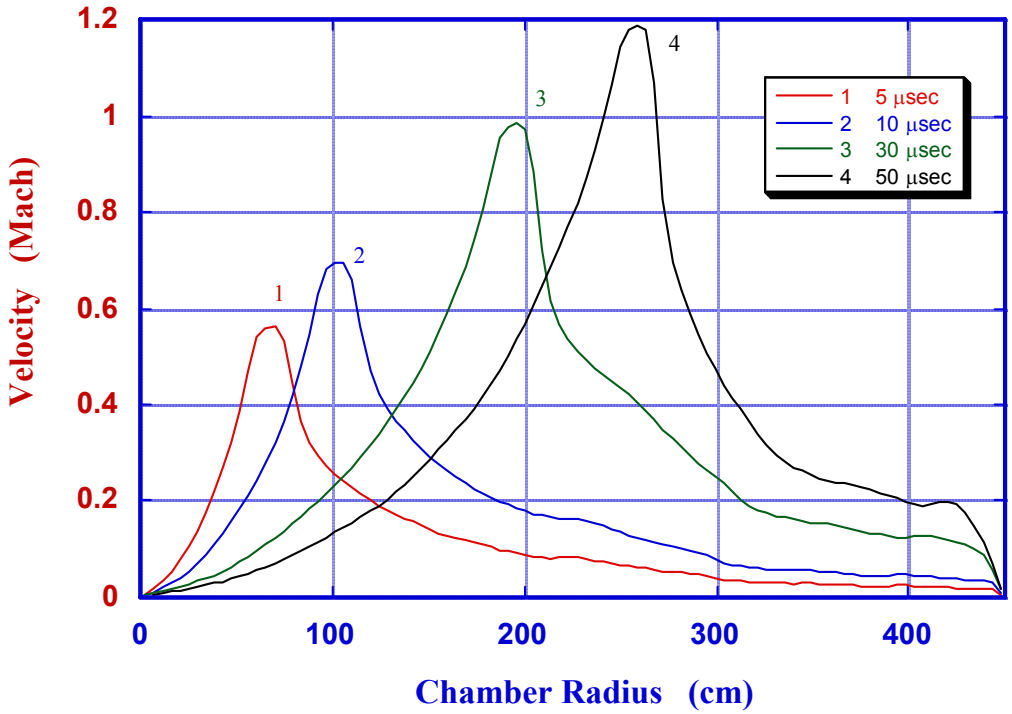

Figure 11 - Generation of supersonic wave in 4.5-m chamber for HIB target (115 MJ) with 0.96 torr Xe

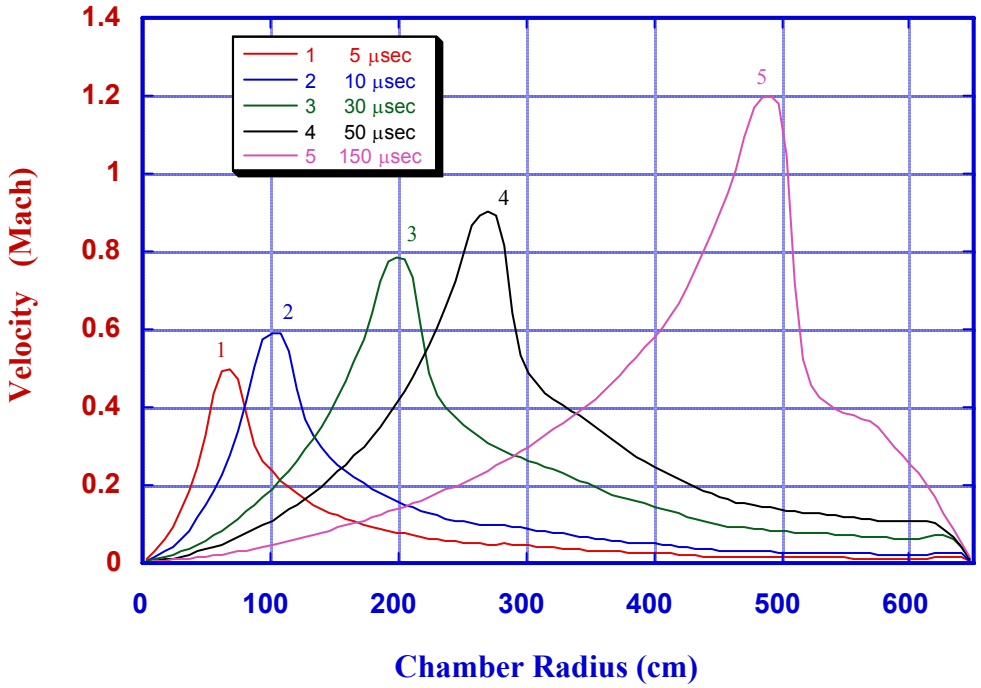

Figure 12 - Generation of supersonic wave in 6.5-m chamber for HIB target (115 MJ) with 0.21 torr Xe

Figure 13 presents the pressure distribution in the high-density case 1. An increase of pressure in the front and decrease after the wave is observed. Figures 14 and 15 show the "classical" case of

spherical explosion without radiation transport [10]. The pressure before the front in the stationary wave is approximately half that after the front. Note that the 300-μsec curve in Fig. 14 is the reflected wave from the wall, and in Fig. 15 it corresponds to interaction with the chamber-wall shock wave. Energy redistribution (case 1) opposes as the final result to gas particle transfer. The peak density diminishes as a result of the motion of the shock wave to the wall (Fig. 16). This decline does not take place in the rarefied Xe (Fig. 17 and 18). The temperature curves differ significantly.

Figure 19 represents the evolution of temperature distribution for the high-density Xe. It shows an area heated by radiation. The local minimums in the curves enable us to evaluate the average free path of the radiation quantum in front of the shock wave. The temperature distributions from Figs. 20 and 21 (cases 2 and 3) do not show natural locally heated areas. The temperature increase in the 300-μsec case (Fig. 20) corresponds to the reflected wave from the chamber wall. Note that, we do not find rapid temperature dispersal in the central area in the case of dense or rarefied gas. That generalization holds when taking into account either hydrodynamic or radiation transport features.

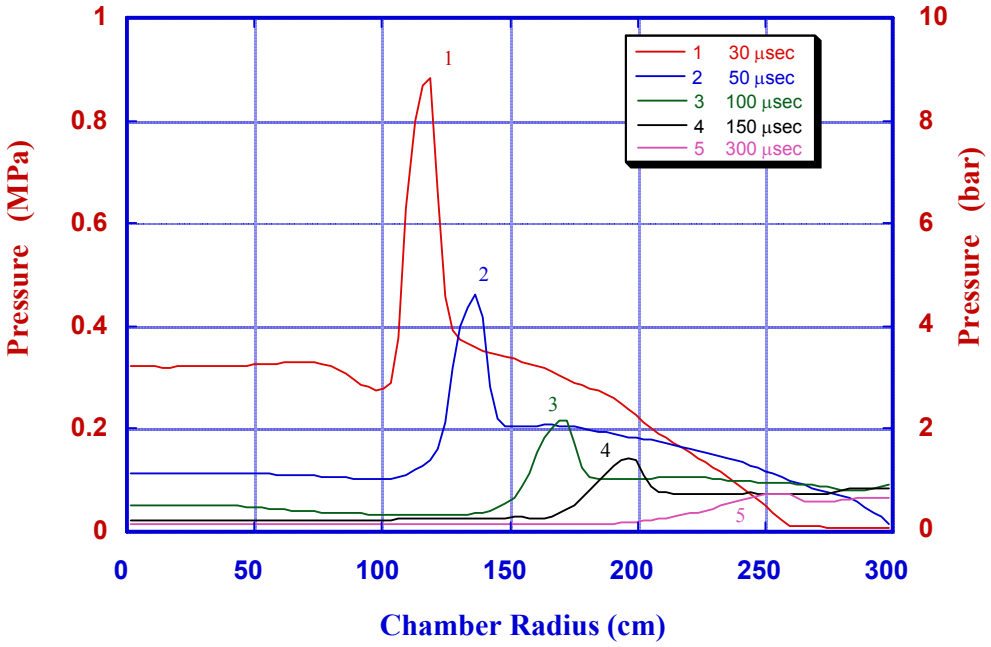

Figure 13 - Pressure evolution in 3-m chamber for HIB target (115 MJ) with 23 torr Xe

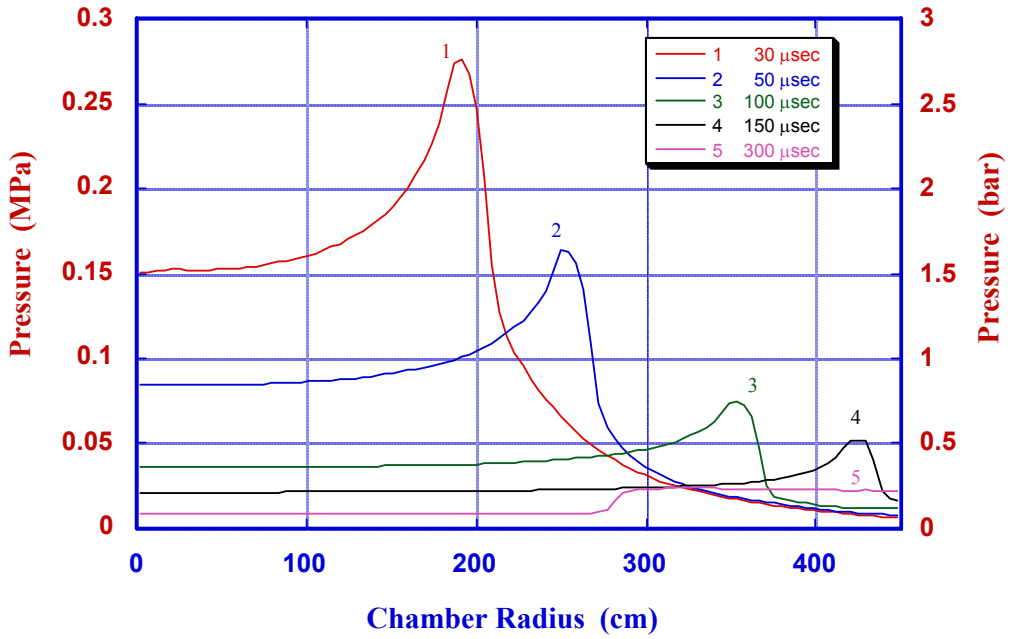

Figure 14 - Pressure evolution in 6.5-m chamber for HIB target (115 MJ) with 23 torr Xe

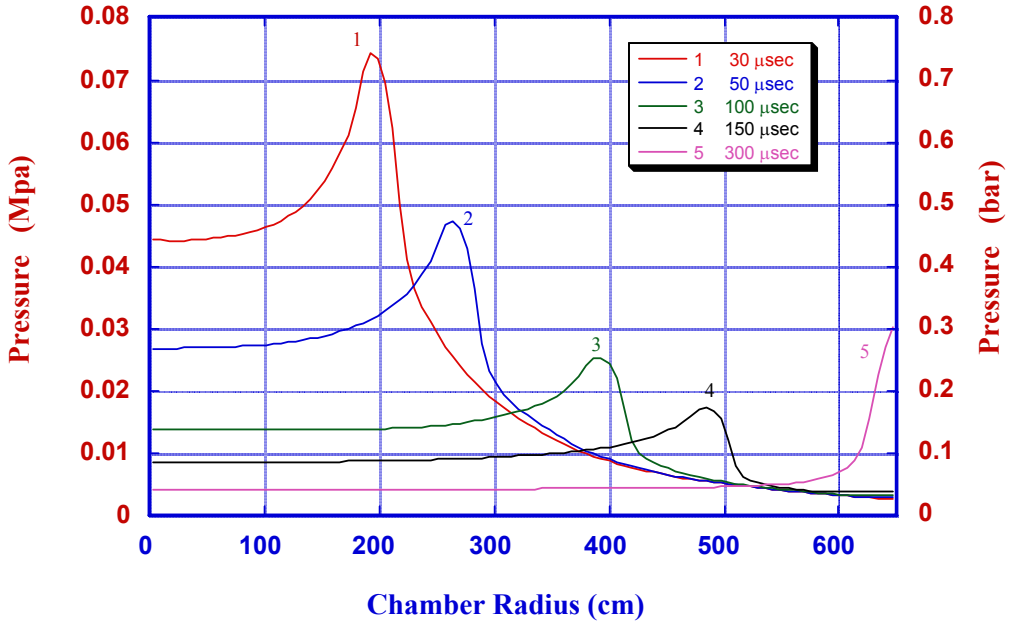

Figure 15 - Pressure evolution in 6.5-m chamber for HIB target (115 MJ) with 0.21 torr Xe

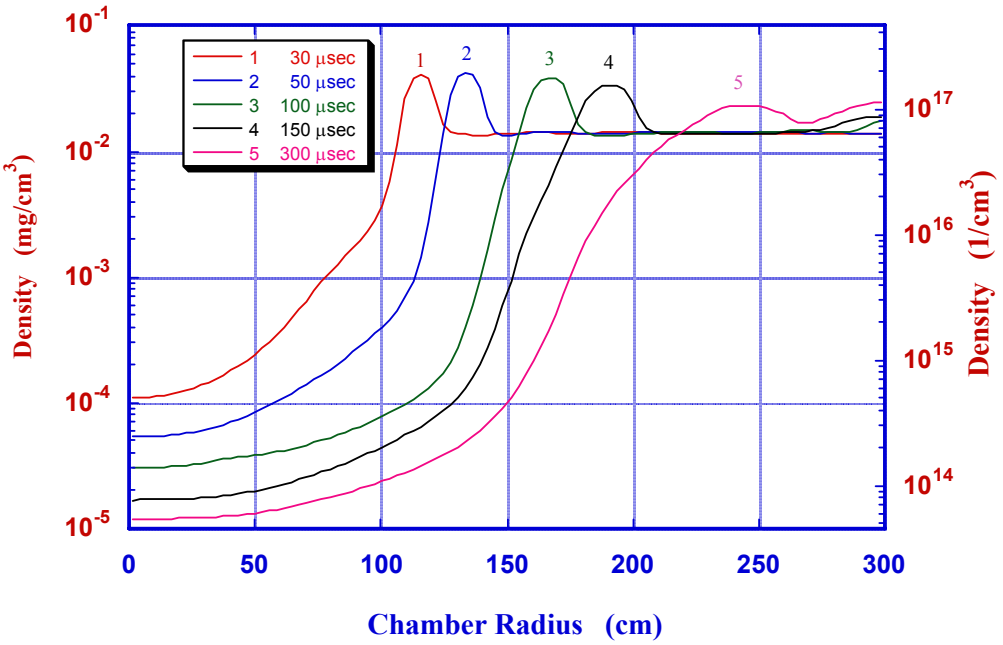

Figure 16 - Density evolution in 3-m chamber for HIB target (115 MJ) with 23 torr Xe

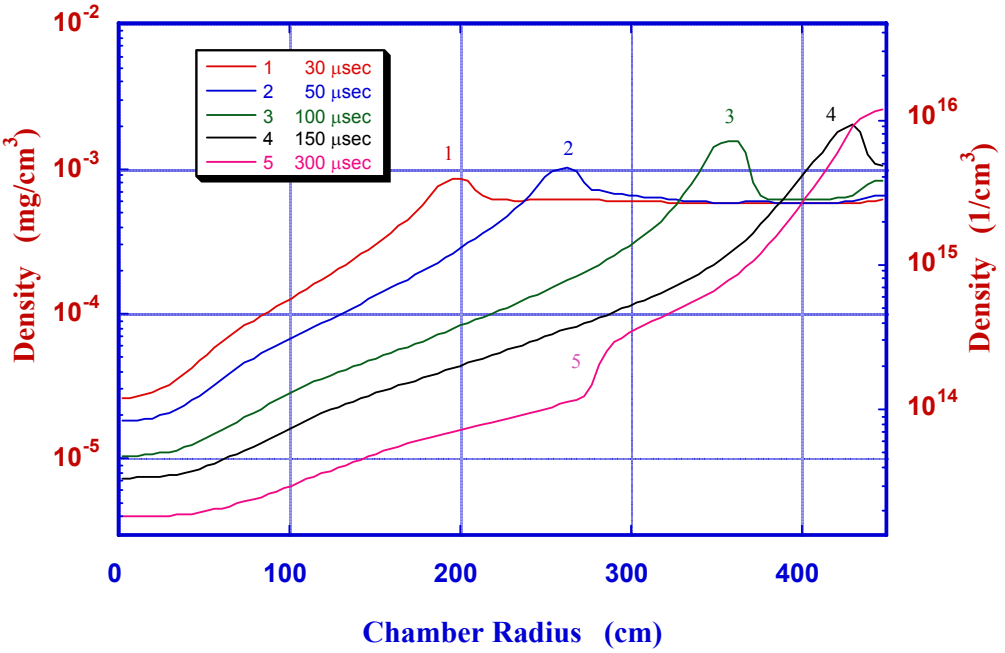

Figure 17 - Density evolution in 4.5-m chamber for HIB target (115 MJ) with 0.96 torr Xe

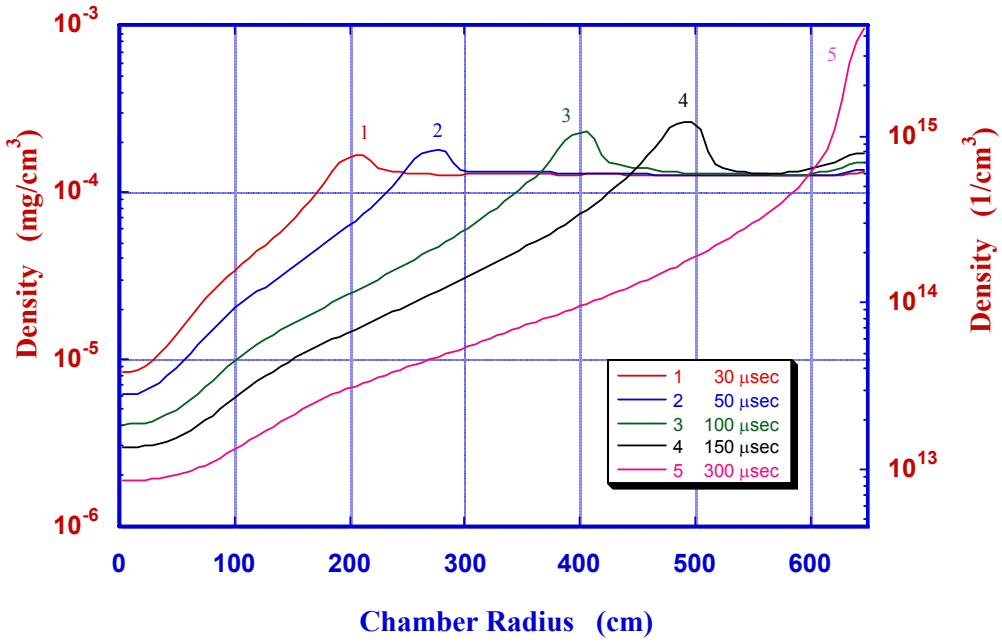

Figure 18 - Density evolution in 6.5-m chamber for HIB target (115 MJ) with 0.21 torr Xe

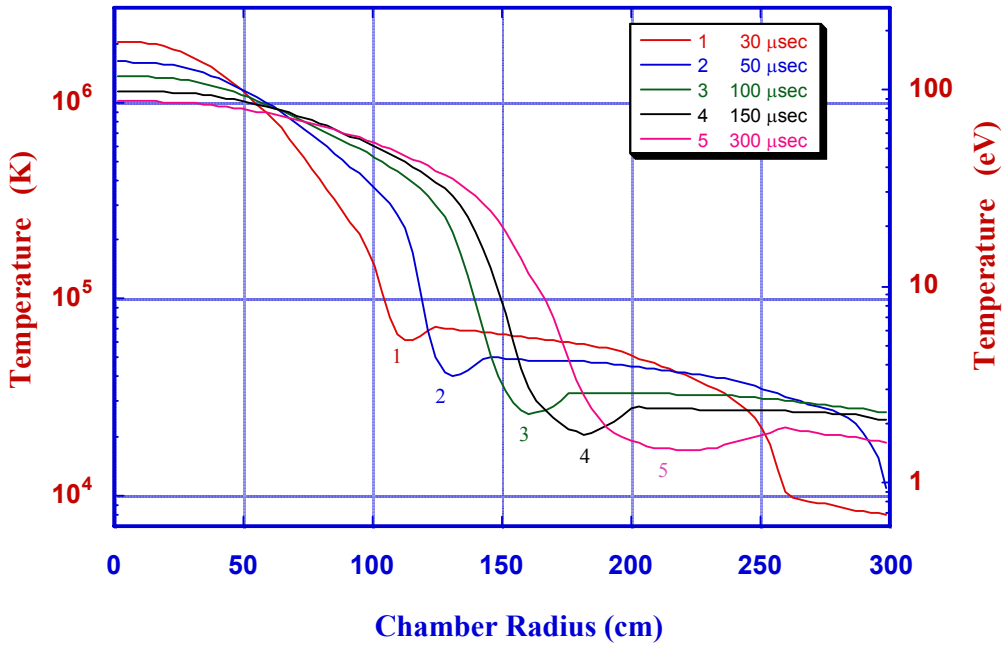

Figure 19 - Gas temperature evolution in 3-m chamber for HIB target (115 MJ) with 23 torr Xe

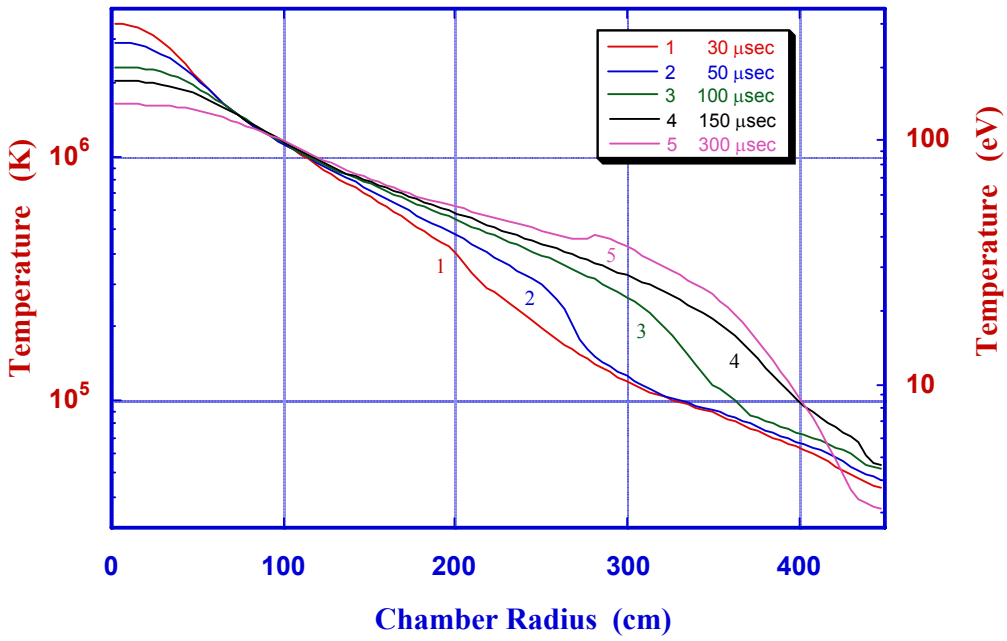

Figure 20 - Gas temperature evolution in 4.5-m chamber for HIB target (115 MJ) with 0.96 torr Xe

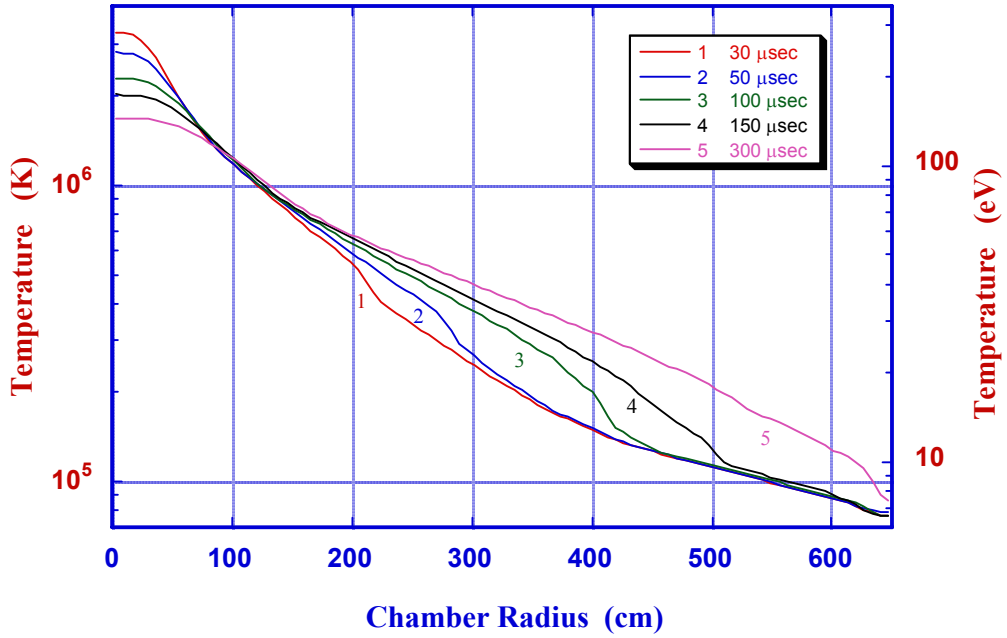

Figure 21 - Gas temperature evolution in 6.5-m chamber for HIB target (115 MJ) with 0.21 torr Xe

5. Results and Discussion

The existence of a shock wave in the chamber influences the dynamics of the accumulation of energy by the wall. Apparently, the less density of the working gas, the higher the first time radiative flow. Figure 22 shows wall radiation vs. flux time curves for all three cases. Case 3 shows the most power for the first-time radiative flow to the wall. By comparison of density it locates nearer to the target (R = 4.5 m), and its square is much lower than that for Case 3. There is an intensive absorption of radiation by the dense Xe gas of the first case. During target implosion, energy is depositing at the chamber center, and the shock wave is being generated. A stable radiative flow starts after the end of target implosion. The radiant energy is highlighted on the wall through a non-perturbed gas layer. The period of constant flux is equal to the passage of time for hydrodynamic perturbation of the first wall. For cases 1, 2, and 3 this time is ~ 50, 150, and 250 μsec, respectively. Note that in case 3, with dense Xe, it is the time for arrival of the warmed area. Direct arrival of the shock wave is indicated by the second local flux maximum at ~450 μsec. A slow decrease of radiative flow starts after interaction of the shock wave and the chamber wall.

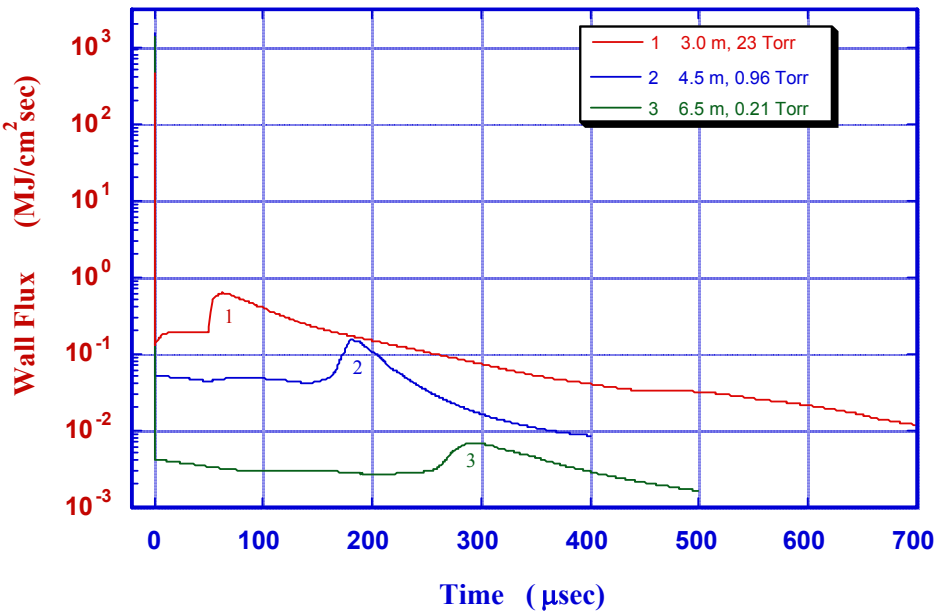

Figure 22 - Evolution of wall radiation flux for different initial conditions.

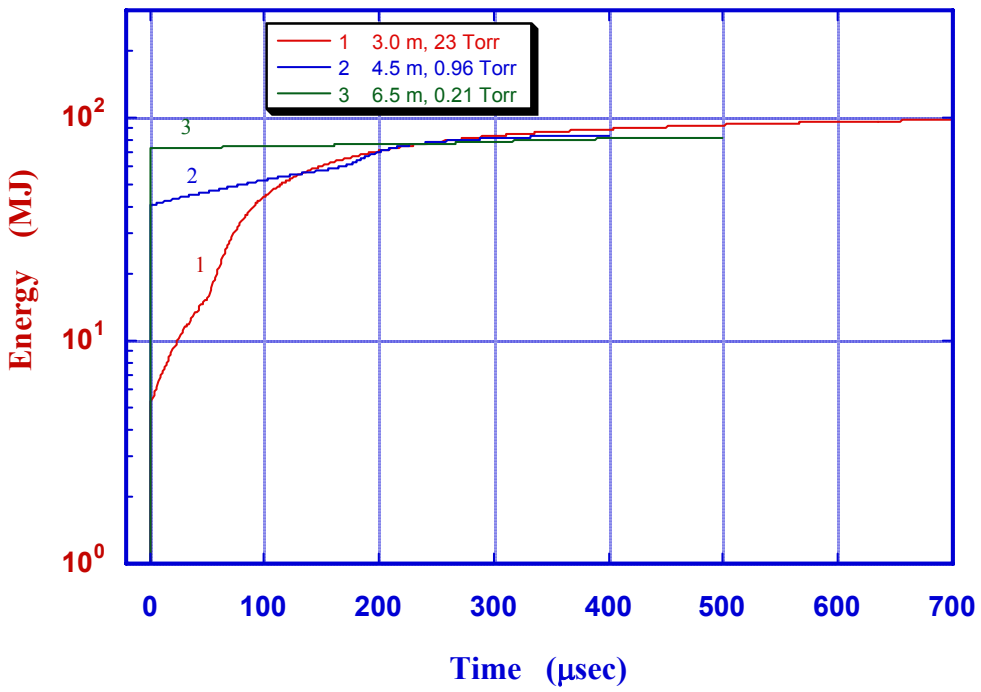

Figure 23 - Evolution of total deposited energy in wall for different initial conditions

Figure 23 shows that behavior of the flux curve shapes the energy accumulation at the first wall. As expected, the greatest first-energy deposition occurs in graphite with the low-density gas. It is approximately ~35% for case 2 (4.5 m, 0.96 torr), and ~63% for case 3 (6.5 m, 0.21 torr). For case 1 (3.0 m, 23 torr), only ~5% of target energy absorbs the wall in the first 10 nsec. However, the dense gas is an effective barrier for radiation energy only in the first ~250 μs. After this time, total energy deposited in the chamber wall is higher, as in the rarefied gas cases. The total energy curve asymptotically approaches the 100 kJ level. Two local peaks are also observed on the pressure-time-curve of the dense gas case (Fig. 24). Comparing Figs. 24 and 13, we conclude that the first peak is mainly caused by the heated area in front of the shock while the second peak is due to the shock wave itself. For the rarefied gas, the shock wave front does not have the pronounced heated area so that the additional peaks do not appear on the appropriate pressure curves.

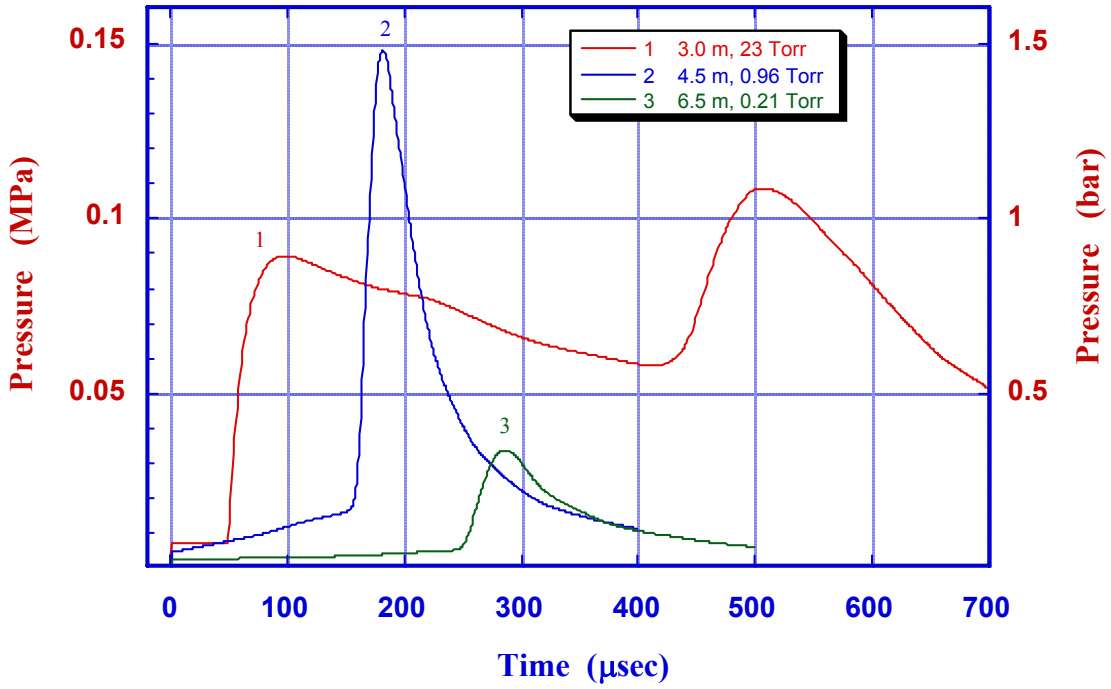

Figure 24 - Evolution of wall pressure for different initial conditions.

The curves reflect only the result of shock wave-wall chamber interaction. Figure 24 indicates an indirect dependence of initial gas pressure (or initial density) on the amplitude of the pressure peak in the chamber wall. Apparently, there are initial conditions for the target at which the amplitude of impact at the first wall reaches a maximum. We have compared our calculated pressure impact on the wall with BUCKY [7] results, (Fig. 25). The BUCKY results do not show the shock wave impact on the curves

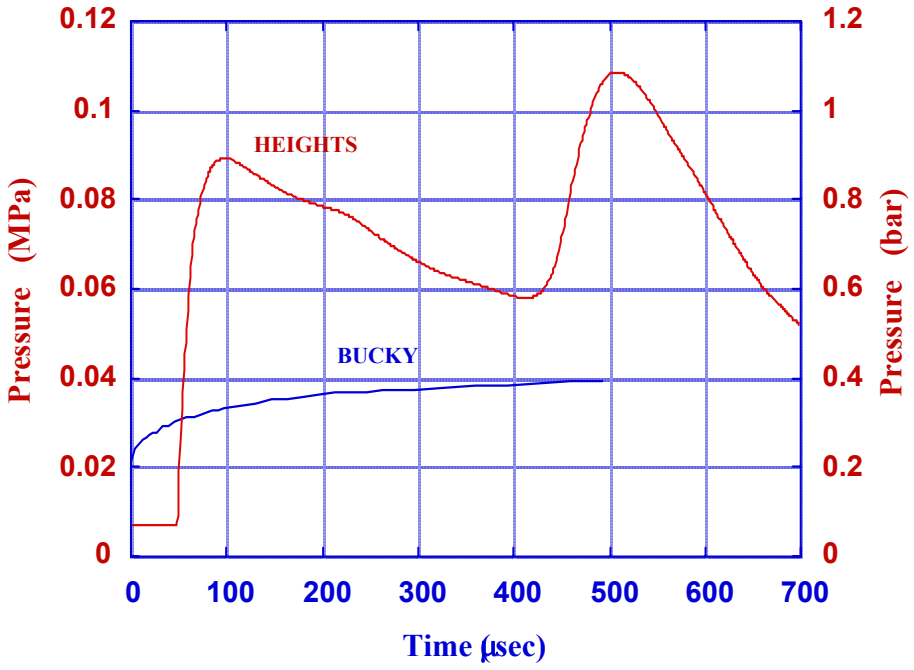

Figure 25 - Evolution of wall pressure vs. time predicted by the HEIGHTS and BUCKY codes for dense gas case

6. Summary

1. Using the TVD numerical method enables accurate calculation of shock wave propagation phenomena.

2. Radiation transport calculated using the "forward-reverse" method was determined to be valid for both optically thin and thick media.

3. Two cases (target implosion in a chamber filled with dense and rarefied Xe gas) were studied.

4. Radiation energy transport from the back to the front of the shock wave was found in the case of the dense gas (23 torr Xe).

5. Hydrodynamics and photon radiation transport calculations were performed, and gas/wall pressure evolution was calculated.

6. In the dense gas case, the hydrodynamic shock wave produced two pressure peaks interacting with the chamber wall. The energy of impact decreased as the amount of radiation redistribution of wave parameters.

7. It is anticipated that the shock wave will have a maximum pressure peak at the wall for a middle density of the studied working gas in the chamber.

8. Calculated results were compared favorably with other published data.

Acknowledgments

Work is supported by the U.S. Department of Energy, Office of Fusion Energy Sciences

References

1. Ya. B .Zeldovich and Yu. P. Raiser, Physics of Shock Wave and High-Temperature Hydrodynamic Phenomena,. V.I, Academic Press, New York, 1966.
2. Gábor Tóth and Duane Odstril, Comparison of Some Flux Corrected Transport and Total Variation Diminishing Numerical Schemes for Hydrodynamic and Magnetohydrodynamic Problems, J. of Comp. Phys., May 1996.
3. Kenneth G Powell et al., A Solution Adaptive Upwind Scheme for Ideal Magnetohydrodynamics, J. Comp. Phys. 154, (1999), 284.
4. P. Janhunden, A Positive Conservative Method for Magnetohydrodynamics Based on HLL and Roe Methods, J. Comp. Phys. V.160 (2000) 649.
5. Gábor Tóth, The $\nabla \cdot B=0$ Constraint in Shock-Capturing Magneto-hydrodynamics Codes, J. Comp. Phys., 161 (2000) 605.
6. http://aries.ucsd.edu/ARIES/WDOCS/ARIES-IFE/SPECTRA/
7. http://fti.neep.wisc.edu/FTI/ARIES/OCT2001/hib_dah.pdf
8. N. Lubimov, and V .V. Rusanov, Gas Flows around Obtuse Bodies (Part I, Calculation Method and Analysis of Flows; Part II, Tables of Gasdynamic Functions), Moscow, 1970.
9. Milton Van Dyke, An Album of Fluid Motion, The Parabolic Press, Stanford, California, 1982.
10. G. Taylor, Proc. Roy. Soc. 201 (1950) 175.

Distribution List for ANL-ET/02-26

Internal:

J.N. Brooks
F. C. Chang
T.H. Chien
H. Drucker
R. Foote (2)
D. Gruen
J. Harmon
A. Hassanein (20)
I. Konkashbaev
C.A. Malefyt
R. Mattas
V. Morozov
J. Norem
R.B. Poeppel
R.C. Schmitt
W. Shack
V.A. Sizyuk (5)
S.W. Tam
V. I. Tolkach
R.A. Valentin
TIS Files

External:
DOE-SC (5)
ANL Libraries:
ANL-E
ANL-W

Main Library:
Brookhaven National Laboratory
Fermi National Accelerator Laboratory
Lawrence Berkeley National Laboratory
Lawrence Livermore National Laboratory
Los Alamos National Laboratory
Naval Research Laboratory
Sandia National Laboratories

Energy Technology Division Review Committee:
H.K. Birnbaum, University of Illinois at Urbana-Champaign
I. -W. Chen, University of Pennsylvania
F. P. Ford, Rexford, N.Y.
S.L. Rohde, University of Nebraska-Lincoln
H.S. Rosenbaum Fremont, CA
S.L. Sass, Cornell University
R. Zoughi, University of Missouri-Rolla

External:
M. Abdou, University of California-Los Angeles
I. Agurok, Physical Optics Corporation-Torrance, CA
M. Akiba, Japan Atomic Energy Research Institute, Japan
J. Anderson, Los Alamos National Laboratory
C. Baker, University of California-San Diego
J. Bartlit, Los Alamos National Laboratory
S. Berk, U.S. Department of Energy
T. Bernat, Lawrence Livermore National Laboratory
G. Besenbruch, General Atomic
C. Bibeau, Lawrence Livermore National Laboratory
D. Bittner, Lawrence Livermore National Laboratory
D. Blackfield, Lawrence Livermore National Laboratory
R. Causey, Sandia National Laboratories-Livermore
D. Colombant, Naval Research Laboratory
B. Cook, Lawrence Livermore National Laboratory
J. Dahlburg, General Atomic
J. Davis, McDonnell Douglas Astronautics Company
S. Dean, Fusion Power Associates
F. Elsner, General Atomic
G. Federici, ITER International Team, Garching, Germany
M. Friedman, Naval Research Laboratory
J. Gardner, Naval Research Laboratory
C. Gentile, Princeton Plasma Physics Laboratory
N. Ghoneim, University of California-Los Angeles
J. Giuliani, Naval Research Laboratory
D. Goodin, General Atomic-San Diego
C. Halvorson, Schafer Laboratories
R. Hawryluk, Princeton Plasma Physics Laboratory
D. Haynes, University of Wisconsin-Madison
F. Hegeler, Naval Research Laboratory
J. Hoffer, Los Alamos National Laboratory
J. Hunn, Oak Ridge National Laboratory
S. A. Khalik, Georgia Tech
W. Kowbel, Materials & Electrochemical Research Corp. (Mercorp)
Y. Kozaki, Osaka University, Japan
G. Kulcinski, University of Wisconsin-Madison
P. Lamarche, Princeton Plasma Physics Laboratory
J. Latkowski, Lawrence Livermore National Laboratory
B. Lehmberg, Naval Research Laboratory
J. Lindl, Lawrence Livermore National Laboratory
Y. Martynenko, Kurchatov Institute, Russia
K. McCarthy, Idaho National Engineering and Environmental Laboratory
R. McKnight, U.S. Department of Energy
W. Meier, Lawrence Livermore National Laboratory

External:(cont)
M. Monsler, Schafer Laboratories- Livermore, CA
M. Myers, Naval Research Laboratory
F. Najmabadi, University of California-San Diego
G. Nardella, U.S. Department of Energy
A. Nobile, Los Alamos National Laboratory
A. Nikro, General Atomic-San Diego
H. Nickel, Kernforschungzentrum, Karlsruhe, Germany
R. Nygren, Sandia National Laboratories-Albuquerque
S. Obenschain, Naval Research Laboratory
C. Olson, Sandia National Laboratories
A. Opdenaker, U.S. Department of Energy
S. Payne, Lawrence Livermore National Laboratory
J. Perkins, Lawrence Livermore National Laboratory
R. Peterson, Los Alamos National Laboratory
D. Petti, Idaho National Engineering and Environmental Laboratory
R. Petzold, General Atomics
F. Powell, Luxel Corporation - Friday Harbor, WA
R. Raffray, University of California-San Diego
T. Renk, Sandia National Laboratories
S. Reyes, Lawrence Livermore National Laboratory
J. Sater, Lawrence Livermore National Laboratory
M. Sawan, University of Wisconsin
S. Searles, Naval Research Laboratory
J. Sethian, Naval Research Laboratory
A. Schmitt, Naval Research Laboratory
R. Schneider, U.S. Department of Energy
D. Schroen, Sandia National Laboratories
A. Schwendt, Los Alamos National Laboratory
K. Schultz, General Atomic
M. Seki, Japan Atomic Energy Research Institute, Japan
P. Sharpe, Idaho National Engineering and Environmental Laboratory
J. Shillito, Schafer Laboratories-Livermore, CA
C. Skinner, Princeton Plasma Physics Laboratory
L. Snead, Oak Ridge National Laboratory
W. Steckle, Los Alamos National Laboratory
D. Steiner, Rensselaer Polytechnic Institute
I. Sviatoslavsky, University of Wisconsin
J. Swadener, Los Alamos National Laboratory
T. Norimatsu, Institute of Laser Engineering, Osaka University, Japan
M. Tillack, University of California, San Diego
Y. Ueda, Osaka University, Japan
M. Ulrickson, Sandia National Laboratories, Albuquerque
J. Van der Laan, ECN, Netherlands
L. Wagner, Boeing, - St. Louis

External:(cont)
X. Wang, University of California-San Diego
D. Weidenheimer, Titan Corporation
M. Wolford, Naval Research Laboratory
S. Zinkle, Oak Ridge National Laboratory

Bibliothek, Max-Planck-Institute für Plasmaphysik, Germany
C.E.A. Library, Fontenay-aux-Roses, France
Librarian, Culham Laboratory, England
Thermonuclear Library, Japan Atomic Energy Research Institute, Japan
University of Wisconsin Library